



# Facile synthesis of Bi/Bi<sub>2</sub>WO<sub>6</sub> nanocomposite with enhanced photocatalytic activity under visible light

Yongkui Huang<sup>a</sup>, Shifei Kang<sup>b</sup>, Yun Yang<sup>c</sup>, Hengfei Qin<sup>a</sup>, Zhijiang Ni<sup>a</sup>, Shuijin Yang<sup>c</sup>, Xi Li<sup>a,\*</sup>

<sup>a</sup> Department of Environmental Science and Engineering, Fudan University, Shanghai 200433, China

<sup>b</sup> School of Environment and Architecture, University of Shanghai for Science and Technology, Shanghai 200093, China

<sup>c</sup> Hubei Collaborative Innovation Center for Rare Metal Chemistry, College of Chemistry and Chemical Engineering, Hubei Normal University, Huangshi 435002, China

## ARTICLE INFO

### Article history:

Received 15 March 2016

Received in revised form 8 May 2016

Accepted 11 May 2016

Available online 12 May 2016

### Keywords:

Bi<sub>2</sub>WO<sub>6</sub>

Metallic Bi

Composite

Photocatalytic activity

## ABSTRACT

Incorporating plasmonic metal nanostructures into semiconductors has been regarded as an effective method to improve the photocatalytic activity for degradation of pollutants in water. In this study, a visible-light-driven photocatalyst Bi/Bi<sub>2</sub>WO<sub>6</sub> was successfully fabricated by a simple two-step route. The samples were systematically characterized by X-ray diffraction, Raman spectroscopy, infrared spectra, field-emission scanning electron microscopy, transmission electron microscopy, X-ray photoelectron spectroscopy, UV–vis diffuse reflection spectroscopy, nitrogen adsorption-desorption isotherms, and photoluminescence spectroscopy. The photocatalytic performance of the Bi/Bi<sub>2</sub>WO<sub>6</sub> composite was evaluated by the photocatalytic decomposition of Rhodamine B and 4-Chlorophenol under visible-light irradiation. The results revealed that the loaded Bi nanoparticles have great influences on the photocatalytic activity of Bi<sub>2</sub>WO<sub>6</sub>. The optimal Bi content for the photocatalytic activity of the Bi/Bi<sub>2</sub>WO<sub>6</sub> composite was determined. Moreover, the photocatalytic mechanism of the degradation processes was thoroughly elucidated. The enhanced photocatalytic performance of the Bi/Bi<sub>2</sub>WO<sub>6</sub> composite should be attributed to the strong visible light absorption, the surface plasmonic resonance (SPR) effect, the high migration efficiency of the electron-holes, and the interfacial interaction between Bi nanoparticles and Bi<sub>2</sub>WO<sub>6</sub>.

© 2016 Elsevier B.V. All rights reserved.

## 1. Introduction

Semiconductor-based photocatalytic oxidation has been recognized as one of the most promising technologies for the environment remediation [1–3]. Titanium dioxide (TiO<sub>2</sub>) based materials have attracted considerable attention in the area of semiconductor photocatalysis [4–6]. However, with large band gaps, TiO<sub>2</sub> can only absorb ultraviolet irradiation, occupying less than 4% of the solar spectrum, and thus restrict its practical applications [3–5,7]. In recent years, visible-light-active photocatalysts have attracted worldwide attention because of their excellent capacity for environmental purification, energy production, and efficient solar-energy utilization [5,8,9].

Bismuth based photocatalysis materials have recently received enormous attention due to its unique band structures and high photocorrosion stability [10–12]. Among them, Bi<sub>2</sub>WO<sub>6</sub> is regarded as an ideal photocatalyst for applications in visible-light driven photocatalysis [11,13]. Generally, the photocatalytic activity of semiconductor is closely related to the morphology, compositions, and structure of the photocatalysts. In this sense, a variety of Bi<sub>2</sub>WO<sub>6</sub> with different morphologies, such as nanoplates [14], nanosheet [15], microsphere [16–18], microdiscs [19], nanobipyramids [20], and other complex morphologies have been prepared to improve its photocatalytic activity. However, the photocatalytic performance of Bi<sub>2</sub>WO<sub>6</sub> is obviously limited by the low efficiency of light absorption, slow rate of charge transfer and the high recombination probability of the photoinduced charge carriers [21–23].

Therefore, many strategies have been adopted to further improve photocatalytic performance of Bi<sub>2</sub>WO<sub>6</sub> [11]. Bulk doping Bi<sub>2</sub>WO<sub>6</sub> nanostructure with element such as Gd [23], Mo

\* Corresponding author.

E-mail address: [xi.li@fudan.edu.cn](mailto:xi.li@fudan.edu.cn) (X. Li).

[24], F [25,26], N [27], is an effective approach for improving the visible-light response. However, these ions tend to decrease the thermal stability and increase the recombination of charge centers of  $\text{Bi}_2\text{WO}_6$  [12,20,28]. On the other hand, the formation of surface defects on the reactive surfaces is an important way to tailor its photocatalytic activities. Surface defects of  $\text{Bi}_2\text{WO}_6$  can strongly impact its chemical and electronic structure [20,29]. These defects could create a miniband just below the conduction band and thus improve the separation efficiency of the photogenerated electron-hole pairs for photocatalytic reactions [28]. Moreover, fabrication of heterojunction system has become an attractive strategy for high performance photocatalytic activity, since it can enlarge the light absorption range and increase the efficient of charge separation, leading to the improved photocatalytic activity and efficiency [12,22,30].

Over the past decade, deposition of plasmonic noble metals on the surface of photocatalysts, which forms a Schottky junction at their interface, have attracted significant research interest due to their extraordinary and tailorable localized surface plasmon resonance (LSPR) properties [31–33]. The noble metal on the photocatalysts helps to enlarge light absorption, separate the photogenerated charge pairs and excite electron-hole pairs in the semiconductors [34,35]. Although the metal nanoparticles loading, such as Au [36], Ag [21,37,38] or Pt [39], can drastically enhance the photocatalytic activity of  $\text{Bi}_2\text{WO}_6$  under visible light irradiation, they are rare and expensive, which severely limits their practical applications [11,40]. In this respect, Bismuth is an attractive alternative because of its much lower material cost and a very small band gap [41–43]. When the Bi nanoparticles are smaller than a few tens of nanometers, a semimetal to semiconductor transition takes place, which results in the LSPR effects [41,44,45]. Recent years, deposition of metallic bismuth (Bi) particles onto semiconductor nanoparticles, such as  $\text{Bi}_2\text{O}_3$  [46],  $\text{TiO}_2$  [44],  $(\text{BiO})_2\text{CO}_3$  [47],  $\text{BiOCl}$  [48,49], and  $\text{BiOCl}_x\text{Br}_{1-x}$  [50], have shown high activities for the degradation of organic contaminants and oxidation of  $\text{NO}_x$  in air. The enhancements are generally attributed to plasmon-induced charge transfer between metallic Bi and semiconductors [47,49,50]. To our knowledge, however, synthesize  $\text{Bi}/\text{Bi}_2\text{WO}_6$  heterostructure nanocatalysts and their photocatalytic activities under visible light irradiation have never been reported so far.

In the present report, a facile, rapid, and environmentally friendly method was developed to synthesize  $\text{Bi}/\text{Bi}_2\text{WO}_6$  heterojunction photocatalysts, which demonstrated high efficiency for photocatalytic degradation organic contaminant.  $\text{Bi}_2\text{WO}_6$  hierarchical microspheres assembled by nanosheets were first synthesized by a facile hydrothermal reaction without using adding any surfactants or capping agents. These microspheres were built by perfectly aligned nanosheets with a lateral size of a few hundred nanometers and thickness of 10–20 nm. Then, Bi nanoparticles with a size of 5–15 nm are uniformly anchored *in situ* onto the surface of  $\text{Bi}_2\text{WO}_6$  nanosheets through a simple solvothermal method. During the reactive process, ethylene glycol has the advantage of mild reducibility compared with traditional reductant, such as  $\text{KBH}_4$ ,  $\text{NaBH}_4$  or ethylene diamine. The photodegradation measurement of Rhodamine B (RhB) and 4-Chlorophenol (4-CP) is used to study the photocatalytic activities of the  $\text{Bi}/\text{Bi}_2\text{WO}_6$  composite under visible light illumination ( $\lambda > 400$  nm). The results demonstrated that the  $\text{Bi}/\text{Bi}_2\text{WO}_6$  composite exhibits much more enhanced photocatalytic activity than metallic Bi and bare  $\text{Bi}_2\text{WO}_6$ . Furthermore, the mechanism of enhanced photocatalytic activity was discussed. It is postulated that the excellent photocatalytic activity of  $\text{Bi}/\text{Bi}_2\text{WO}_6$  should be ascribed to synergetic effect of Bi nanoparticles and  $\text{Bi}_2\text{WO}_6$ .

## 2. Experimental

### 2.1. Preparation of the $\text{Bi}/\text{Bi}_2\text{WO}_6$ photocatalysts

$\text{Bi}_2\text{WO}_6$  microspheres were first prepared via a modified method reported elsewhere [18,37]. In typical procedure,  $\text{Bi}(\text{NO}_3)_3 \cdot 5\text{H}_2\text{O}$  (2 mmol) was dissolved in a 50 mL aqueous solution containing 1 mmol of nitric acid to form a clear solution. Meanwhile,  $\text{Na}_2\text{WO}_4 \cdot 2\text{H}_2\text{O}$  (1 mmol) was dissolved in 40 mL deionized water under constant stirring. After that, the  $\text{Na}_2\text{WO}_4$  aqueous solution was dropped into the  $\text{Bi}(\text{NO}_3)_3$  aqueous solution slowly. After being stirred for 2 h, the suspension was transferred into a 120 mL Teflon-lined stainless steel autoclave up to 75% of the total volume. The autoclave was sealed and heated at  $160^\circ\text{C}$  for 24 h, then cooled to room temperature naturally. The precipitates were washed for several times with deionized water and absolute ethyl alcohol, respectively. Then, the sample was dried in a vacuum at  $60^\circ\text{C}$  for 24 h.

$\text{Bi}/\text{Bi}_2\text{WO}_6$  composites were prepared by the growth of Bi on the surfaces of  $\text{Bi}_2\text{WO}_6$  using EG as solvent and reducing agent under solvothermal conditions. Typically, 0.2 mmol  $\text{Bi}(\text{NO}_3)_3 \cdot 5\text{H}_2\text{O}$  was dissolved in 80 mL ethylene glycol to form a transparent solution. Then 0.42 g  $\text{Bi}_2\text{WO}_6$  powder was added into the above solution with ultrasonic dispersion for 10 min and vigorously stirred for a further 2 h to form the suspension. The suspension was transferred to a Teflon-lined stainless steel autoclave and then heated in an electric oven at  $180^\circ\text{C}$  for 10 h. The obtained raw products were separated by centrifuge, washed several times with deionized water and ethanol, and dried at  $60^\circ\text{C}$  for 12 h. Finally, the  $\text{Bi}/\text{Bi}_2\text{WO}_6$  composite was obtained. The continuously variable concentrations of Bi in  $\text{Bi}/\text{Bi}_2\text{WO}_6$  nanostructures could be attempted by controlling the ratio of  $\text{Bi}(\text{NO}_3)_3 \cdot 5\text{H}_2\text{O}$  and  $\text{Bi}_2\text{WO}_6$  in the solution. The contents of Bi in  $\text{Bi}/\text{Bi}_2\text{WO}_6$  were 1.0, 2.0, 5.0, and 9.5% by mass ratio. The corresponding products were marked as 1.0, 2.0, 5.0, and 9.5%  $\text{Bi}/\text{Bi}_2\text{WO}_6$ , respectively.

### 2.2. Materials characterization

The crystalline structures of the samples were characterized by a powder X-ray diffraction (XRD) using a Bruke D8 Advance powder X-ray diffractometer with  $\text{Cu K}\alpha$  ( $\lambda = 0.15406$  nm). The morphologies and microstructures characterizations were performed on the field-emission scanning electron microscopy (FESEM, Zeiss, Ultra-55) and field-emission transmission electron microscopy (FETEM, JOEL JEM 2100F). The chemical composition was investigated by the energy-dispersive X-ray spectroscopy (EDX). Raman spectra were obtained using the LabRam-1B system from Horiba Jobin Yvon at room temperature with a 532 nm solid laser as the exciting source. Fourier transformation infrared spectra (FT-IR) were acquired in the range  $400\text{--}4000\text{ cm}^{-1}$  with a NICOLET 5700 FTIR spectrometer. X-ray photoelectron spectroscopy (XPS) was performed using a RBD upgraded PHI-5000C ESCA system (Perkin Elmer) with  $\text{Mg K}\alpha$  radiation ( $h\nu = 1253.6$  eV). The binding energy data was calibrated with the C 1s signal at 284.6 eV. UV-vis absorption spectra were recorded on a UV-vis spectrophotometer (UV-2550, Shimadzu) with an integrating sphere attachment. The analysis range was 250–800 nm, and  $\text{BaSO}_4$  was used as a reflectance standard. Nitrogen adsorption-desorption isotherm measurements were performed on a Micromeritics ASAP 2020 and the bath temperature was 77.35 K. Photoluminescence (PL) spectrum was obtained on an Edinburgh FLS 920 fluorescence spectrophotometer. All the spectra were taken at room temperature with an excitation wavelength of 300 nm.

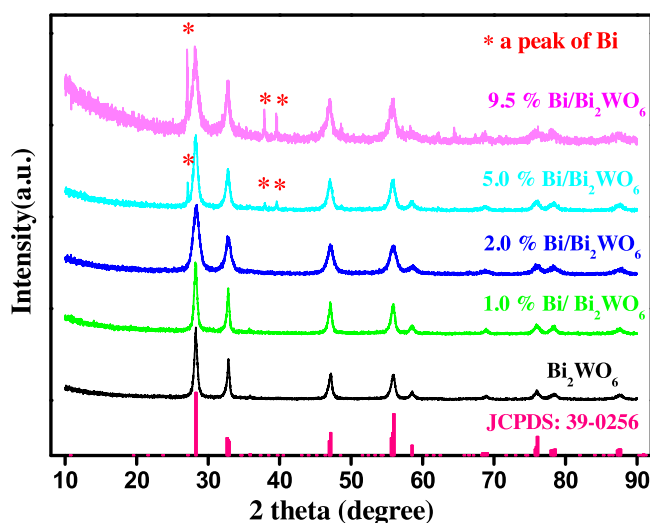


Fig. 1. XRD patterns of the Bi/Bi<sub>2</sub>WO<sub>6</sub> composites.

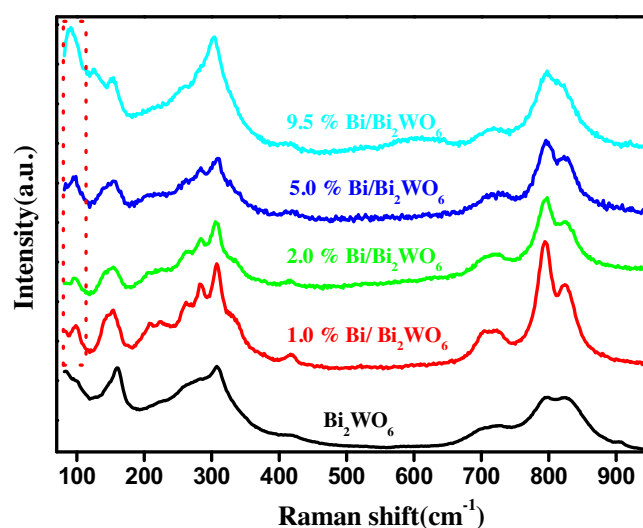


Fig. 2. Raman spectrum of the Bi/Bi<sub>2</sub>WO<sub>6</sub> composites.

### 2.3. Photocatalytic evaluation

Photocatalytic reactions were carried out in a photoreaction vessel containing an aqueous solution of RhB under visible light irradiation. All the experiments were carried out in a glass reactor, in which 50 mg of catalysts was added into 50 mL of RhB solution with an initial concentration of 10 mg L<sup>-1</sup>. A 300 W Xe lamp (PLS-SXE300C, Beijing Perfect Light Co. Ltd, Beijing) was used as a light source, and a 400 nm cutoff filter was placed above the reactor to cut off the UV light, whose intensity of incident light was 200 mW cm<sup>-2</sup> (CEL-NP2000 Light Power Meter, Beijing Aulight Co. Ltd, China). Prior to irradiation, the pollutant solution with photocatalyst were magnetically stirred in dark for 30 min to ensure the establishing of an adsorption/desorption equilibrium. The solution was then exposed to the visible light irradiation. The reaction vessel was kept under a water jacket to keep the whole reaction system maintaining at a constant room temperature (25 °C). At given time intervals, 2 mL aliquots were collected from the suspension and immediately centrifuged, the concentration of RhB after illumination was determined using a UV–vis spectrophotometer (Unico UV-4802).

To detect the active species generated during photocatalytic reactivity, various scavengers were added into the solution of RhB. The disodium ethylenediaminetetraacetate (EDTA) is applied as holes ( $h^+$ ) scavenger, *p*-benzoquinone (BZQ) as superoxide radicals ( $\text{O}_2^{\cdot-}$ ) radical scavenger and *tert*-butyl alcohol (TBA) as hydroxyl radicals ( $\text{OH}^{\cdot}$ ) scavenger. The reaction conditions were similar to the photodegradation reactions except that additional radical scavengers (1 mM) were added into the reaction mixture.

The reproducibility of the photocatalyst was also tested with the following procedure: the photocatalyst was washed with ultra-pure water and ethanol for several times after the photodegradation reaction, and then retested in the fresh mixture solution of pollutants solution under the same experimental conditions as mentioned above.

## 3. Results and discussion

### 3.1. Characterizations of samples

The crystal structures of the samples were investigated by the XRD method. As shown in Fig. 1, the diffraction peaks of the pure Bi<sub>2</sub>WO<sub>6</sub> sample at  $2\theta$  values of 28.3, 32.9, 47.2, 56.0, 58.5, 76.1, 78.5, and 87.7° have been observed, which matched well with the

(1 3 1), (0 0 2), (2 0 2), (1 3 3), (2 6 2), (2 10 2), (2 0 4), and (2 10 3) planes of the orthorhombic structure (JCPDS card 39-0256), respectively. There is no trace of any impurity phase, indicating the high purity of the as-prepared samples. For the Bi/Bi<sub>2</sub>WO<sub>6</sub> composites, all the Bi<sub>2</sub>WO<sub>6</sub> diffraction peaks were found at Bi/Bi<sub>2</sub>WO<sub>6</sub> composites, thus indicating that the deposition of Bi nanoparticles did not affect the crystalline structure of Bi<sub>2</sub>WO<sub>6</sub>. Additionally, the weak diffraction peaks (20) at 27.2, 38.0, and 39.7° were founded, which can be assigned to (0 1 2), (1 0 4), and (1 1 0) crystal phases of metallic Bi (JCPDS card 44-1246). Meanwhile, the diffraction peaks intensity of metallic Bi become stronger with the increase of metallic Bi content, while the characteristic peaks of Bi<sub>2</sub>WO<sub>6</sub> decrease in intensity. Notably, no diffraction peaks for metallic Bi can be observed in the nanocomposites of 1.0 and 2.0% Bi/Bi<sub>2</sub>WO<sub>6</sub> samples, which might be due to the low amount and high dispersion of metallic Bi nanoparticles in the composites.

Raman spectra of the samples are shown in Fig. 2. For the Bi<sub>2</sub>WO<sub>6</sub>, several peaks in the range of 600–1000 cm<sup>-1</sup> in the Raman spectrum are assigned to the stretching of the W–O band [51]. In detail, the peaks at 795 and 827 cm<sup>-1</sup> are attributed to antisymmetric and symmetric Ag modes of the O–W–O group terminus, respectively. The peak at 308 cm<sup>-1</sup> is assigned to the translation modes involving simultaneous motions of Bi<sup>3+</sup> and WO<sub>6</sub><sup>6-</sup>. The intensity of the peak at 727 cm<sup>-1</sup> is interpreted as an antisymmetric bridging mode associated with the tungstate chain. For Bi/Bi<sub>2</sub>WO<sub>6</sub> samples, new bands located at 96 cm<sup>-1</sup> appeared, which can be definitely attributed to the first-order scattering A1g modes of Bi [46]. Meanwhile, it should be pointed out that the intensities of some peaks around 308 cm<sup>-1</sup> and the peak at 827 cm<sup>-1</sup> decrease step by step with the Bi content increasing. The results demonstrated the existence of metallic Bi on the Bi<sub>2</sub>WO<sub>6</sub> surface and strong interaction between metallic Bi and Bi<sub>2</sub>WO<sub>6</sub>.

In order to further confirm the composition of the as-prepared samples, pure Bi<sub>2</sub>WO<sub>6</sub> and Bi/Bi<sub>2</sub>WO<sub>6</sub> composites were characterized by FT-IR analysis (Fig. S1). The small peak existing at 1643 cm<sup>-1</sup> is attributed to bending vibrations of O–H, which indicates Bi<sub>2</sub>WO<sub>6</sub> nanosheets contain the hydroxyl groups. The peak at 734 cm<sup>-1</sup> and 1384 cm<sup>-1</sup> are attributed to W–O stretching and W–O–W bridging stretching modes, which indicating the existence of Bi<sub>2</sub>WO<sub>6</sub> [22,52]. The absorption band at 567 cm<sup>-1</sup> is assigned to the Bi–O stretching mode. However, the characteristic peak of Bi–O becomes weak with the introduction of metallic Bi, indicating that an interface interaction between Bi and Bi<sub>2</sub>WO<sub>6</sub>.



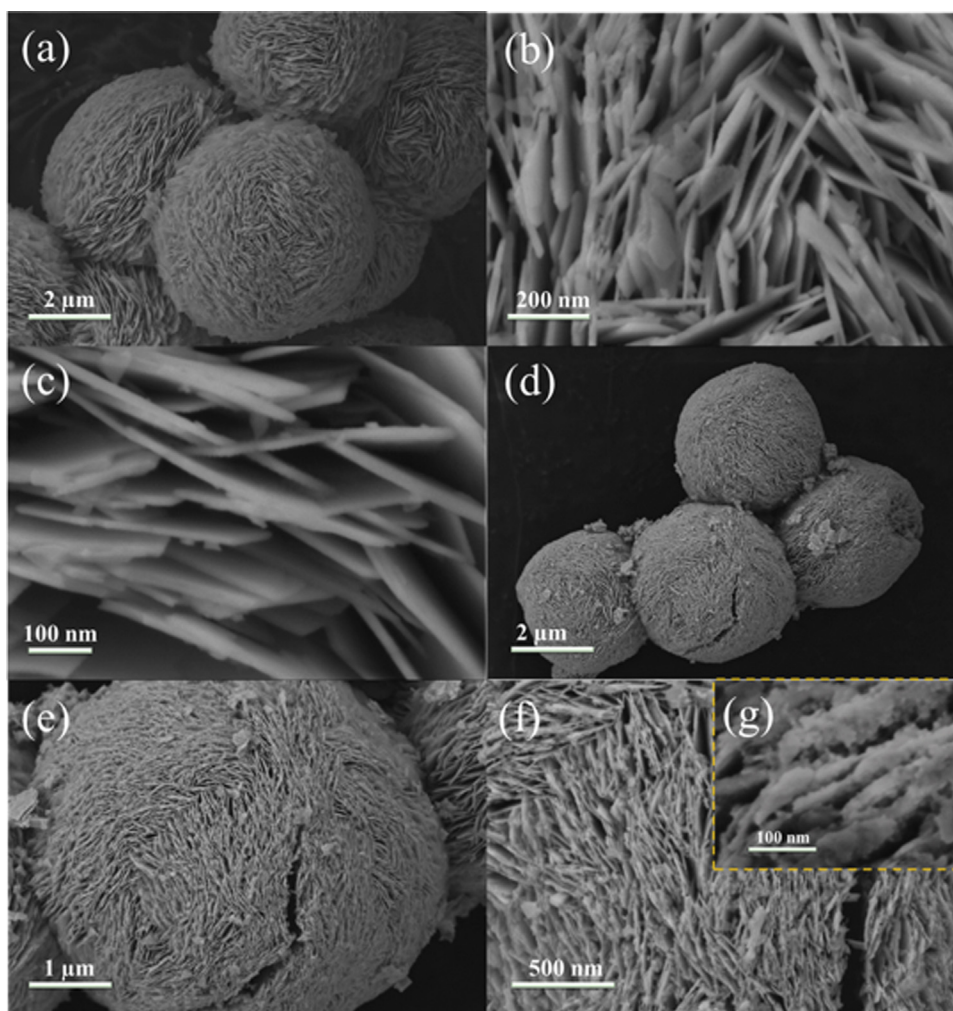


**Fig. 3.** FESEM images of the  $\text{Bi}_2\text{WO}_6$  (a–c) and 5.0%  $\text{Bi}/\text{Bi}_2\text{WO}_6$  composite (d–g).

The morphologies of pure  $\text{Bi}_2\text{WO}_6$  and 5.0%  $\text{Bi}/\text{Bi}_2\text{WO}_6$  samples were further studied using FE-SEM. It can be clearly seen from Fig. 3a and b that the pure  $\text{Bi}_2\text{WO}_6$  present flower-like microspheres constructed from many 2D interlaced nanosheets and their average particle size is in the range of 3–5  $\mu\text{m}$ . The high-magnification SEM image (Fig. 3c) indicated that these superstructures are in fact built from densely packed 2D nanosheets with a thickness of about 10–20 nm. These nanosheets are intercrossed each other and aggregated together to form flower-like microspheres with very smooth surfaces. This could provide more active points for the adsorption of organic pollutants and enhance the photocatalytic activity of the sample. The SEM images of the 5.0%  $\text{Bi}/\text{Bi}_2\text{WO}_6$  composite were shown in Fig. 3d–g, which clearly indicate that the sample maintained similar sizes and hierarchical architectures to the  $\text{Bi}_2\text{WO}_6$  flower-like microspheres. Moreover, many nanoparticles were observed, which are anchored on the nanosheet surface, and these nanoparticles were confirmed to be metallic Bi particles in the following discussion.

To further confirm the composition of the composite, the 5.0%  $\text{Bi}/\text{Bi}_2\text{WO}_6$  sample was characterized by TEM. As shown in Fig. 4, the microspheres were formed from the assemblies of many arranged 2D interlaced nanosheets, which is consistent with the above SEM images. According to TEM images, Bi nanoparticles have different sizes with diameters ranging from 5 to 15 nm. These particles are well separated from each other and spread out on the surface of  $\text{Bi}_2\text{WO}_6$ . By measuring the lattice fringes, the fringe spacing are

about 0.328 and 0.270 nm, which correspond to the (0 1 2) crystal plane of metallic Bi and (0 0 2) lattice plane of  $\text{Bi}_2\text{WO}_6$ , respectively. These observations clearly indicated that Bi nanoparticles are coated on the surface of  $\text{Bi}_2\text{WO}_6$ , which provide the possibility to rectify the photocatalytic performance of composites under the visible light. Furthermore, the EDS patterns in Fig. S2 indicate that the sample only contains Bi, O and W elements. According to further analysis, the atomic molar ratio of Bi:W is approximately 2.37:1, which is higher than that of  $\text{Bi}_2\text{WO}_6$ . This result further indicates that metallic Bi nanoparticles are actually deposited on the surface of  $\text{Bi}_2\text{WO}_6$ , which is consistent with the XRD and Raman data.

X-ray photoelectron spectroscopy (XPS) was further performed to investigate the surface chemical composition and chemical states of the 5.0%  $\text{Bi}/\text{Bi}_2\text{WO}_6$  composite. The XPS survey spectra in Fig. 5a reveals that the sample is mainly composed of Bi, W, O, and a trace amount of C elements (C element come from the reference sample). Fig. 5b shows high resolution Bi 4f XPS spectra of the sample. The peaks at 159.0 eV and 164.4 eV are observed, which could be ascribed to  $\text{Bi } 4f_{7/2}$  and  $\text{Bi } 4f_{5/2}$ , respectively [22,52]. These two peaks can be further deconvoluted into two sets of peaks at 159.0, 164.4 eV, and 157.2, 162.5 eV, respectively. Those at 159.0 and 164.4 eV are ascribed to the  $\text{Bi}^{3+}$  species of pristine  $\text{Bi}_2\text{WO}_6$ , while those at 157.2 and 162.5 eV belong to the  $\text{Bi } 4f_{7/2}$  and  $\text{Bi } 4f_{5/2}$ , respectively [50]. Moreover, based on quantitative results areas, the molar ratio of metallic Bi species to total Bi is calculated to be 2.5%, which is very close to the experimental design value (2.6%).

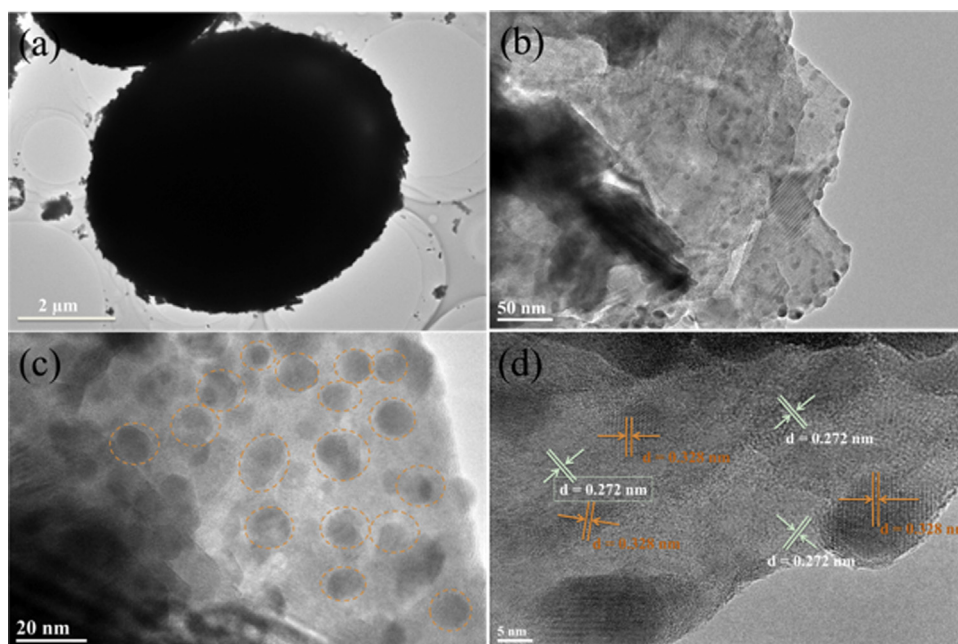


Fig. 4. TEM (a–c) and HRTEM (d) images of the 5.0% Bi/Bi<sub>2</sub>WO<sub>6</sub> sample.

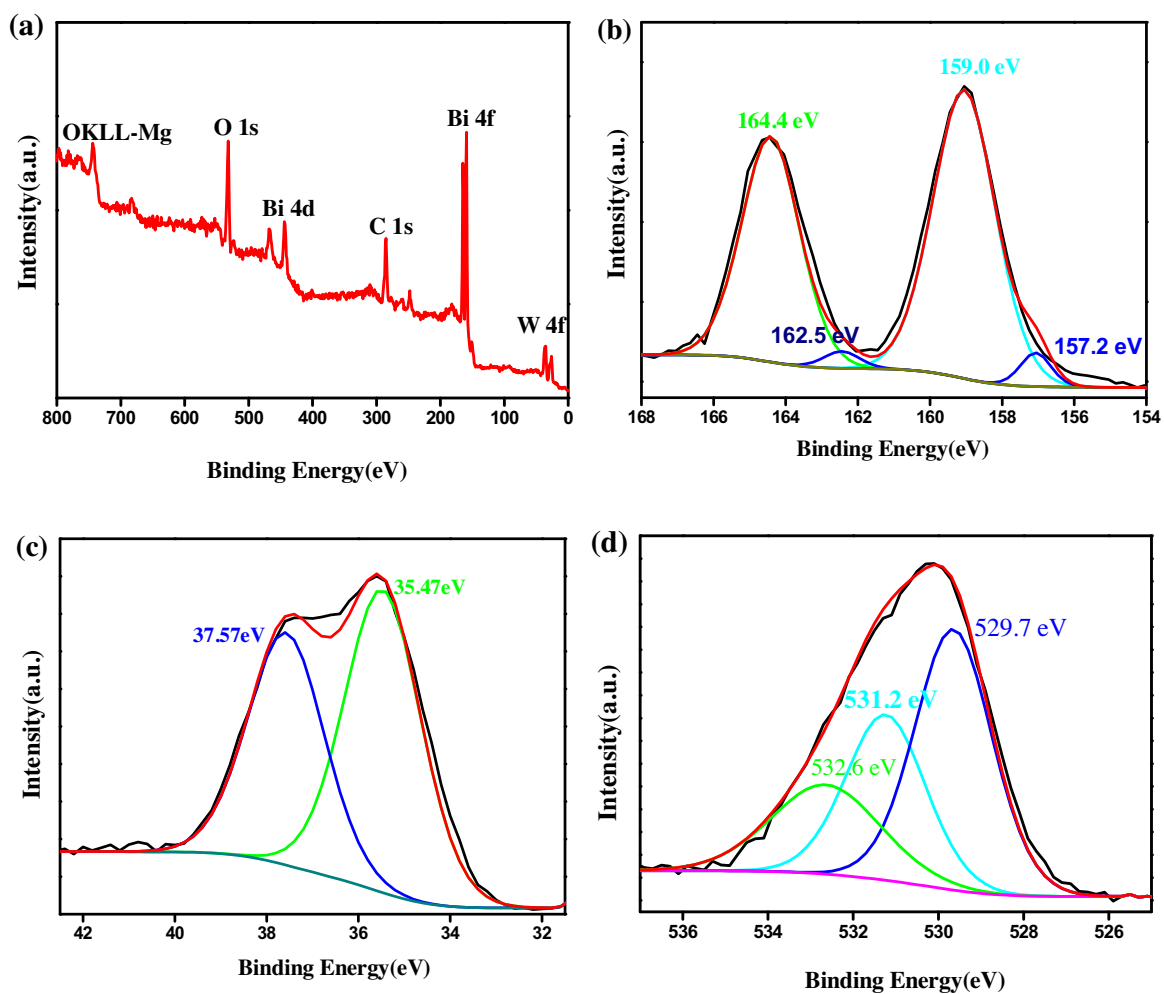


Fig. 5. XPS spectrum of the 5.0% Bi/Bi<sub>2</sub>WO<sub>6</sub> sample. (a) survey scan, (b) Bi 4f, (c) W 4f, and (d) O 1s.

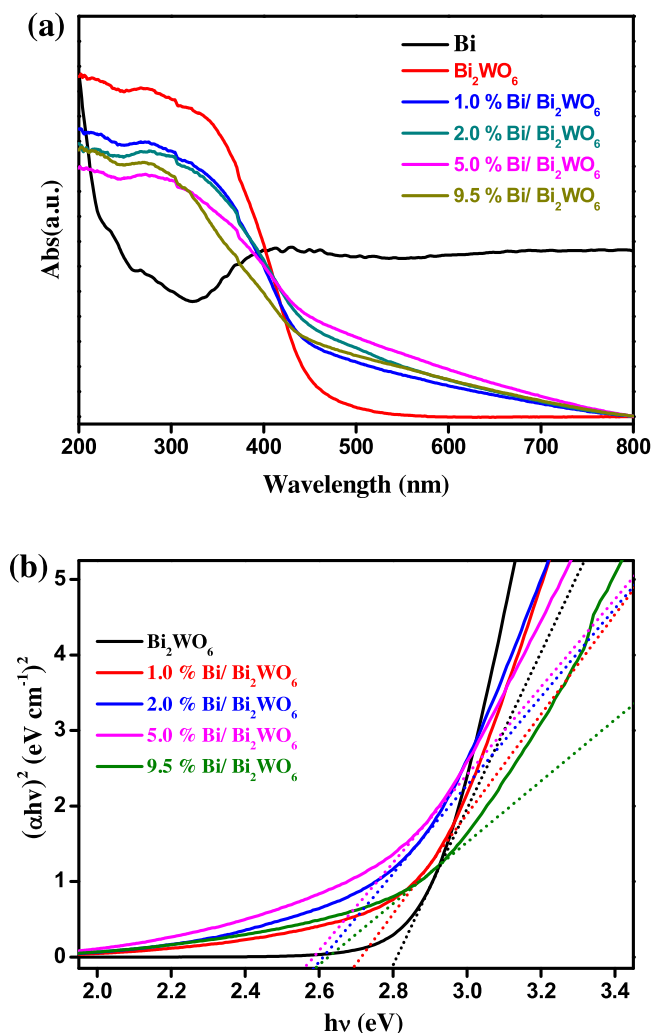


Fig. 6. UV-vis diffuses reflectance spectra (a) and band gaps (b) of the Bi/Bi<sub>2</sub>WO<sub>6</sub> composites.

As shown in Fig. 5c, the two peaks at 37.5 and 35.4 eV are assigned to W 4f<sub>5/2</sub> and W 4f<sub>7/2</sub>, respectively, which are the features of W species in the WO<sub>6</sub> octahedron [12,52]. The XPS spectrum in the O 1s region can be fitted into three peaks (Fig. 5d), positioned at 529.7, 531.2, and 532.6 eV, which are assigned to crystal lattice oxygen [Bi<sub>2</sub>O<sub>2</sub>]<sup>2+</sup> and [WO<sub>4</sub>]<sup>2-</sup> layers of Bi<sub>2</sub>WO<sub>6</sub> and the adsorbed oxygen in the form of hydrated species OH on the surface, respectively [29,53]. Therefore, combining XRD, Raman, SEM and TEM analyses, the results confirm the existence of metallic Bi and Bi<sub>2</sub>WO<sub>6</sub> in the sample, further indicating the formation of Bi/Bi<sub>2</sub>WO<sub>6</sub> heterojunction structure.

The optical absorption of pure Bi<sub>2</sub>WO<sub>6</sub> and Bi/Bi<sub>2</sub>WO<sub>6</sub> composites were measured using a UV-vis diffuse reflectance spectrometer, as shown in Fig. 6a. The absorption peak at 340–800 nm can be observed for pure Bi nanoparticles, which is assigned to the surface plasmon resonance (SPR) of metallic Bi. This phenomenon has also been reported by other groups [47,50]. The absorption edge of pure Bi<sub>2</sub>WO<sub>6</sub> is estimated to be 464 nm, which agrees well with the reported values [30,54]. The considerable visible light absorption of Bi<sub>2</sub>WO<sub>6</sub> is attributed to the transition from the hybrid orbital of O 2p and Bi 6s to the W 5d orbital [30]. For the Bi/Bi<sub>2</sub>WO<sub>6</sub> composites, the absorption within the visible light range apparently increased and a red shift appeared compared with pure Bi<sub>2</sub>WO<sub>6</sub>. The intensity of light absorption of the Bi nanoparticles is somewhat lower, which can be ascribed to the low spatial density of Bi nanoparticles on the surface of Bi<sub>2</sub>WO<sub>6</sub>, and interaction between

Bi nanoparticles and Bi<sub>2</sub>WO<sub>6</sub>. However, it can be clearly seen that Bi/Bi<sub>2</sub>WO<sub>6</sub> composites with different metallic Bi contents showed different absorption abilities, and 5.0% Bi/Bi<sub>2</sub>WO<sub>6</sub> has the most obvious red shift in the absorption edge in comparison with other samples. So, the enhanced light absorption should be attributed to the introduction of metallic Bi nanoparticles [46,50]. The band gap energies of the samples were estimated from the plots of (αhν)<sup>2</sup> versus the energy of absorbed light [53]. As can be seen from Fig. 6b, the estimated band gap values of the samples are approximately 2.76, 2.68, 2.58, 2.55, and 2.58 eV for samples of pure Bi<sub>2</sub>WO<sub>6</sub>, 1.0, 2.0, 5.0, and 9.5% Bi/Bi<sub>2</sub>WO<sub>6</sub>, respectively. This result suggests that the metallic Bi deposition can slightly lower the apparent band gap of the whole composite [46,50].

### 3.2. Photocatalytic activity

The photocatalytic performances of the Bi/Bi<sub>2</sub>WO<sub>6</sub> composites were evaluated by the degradation of environmental pollutants under visible light irradiation. RhB, a chemically stable molecule, was firstly chosen as a representative model pollutant to evaluate the photocatalytic performance of samples. For comparison, degradation of RhB on commercial TiO<sub>2</sub> (P25), metallic Bi, and pure Bi<sub>2</sub>WO<sub>6</sub> was also performed under the other identical conditions, respectively. As shown clearly in Fig. 7a, RhB is only slightly degraded in the absence of photocatalysts, indicating that the degradation under direct photolysis can be ignored. In addition,

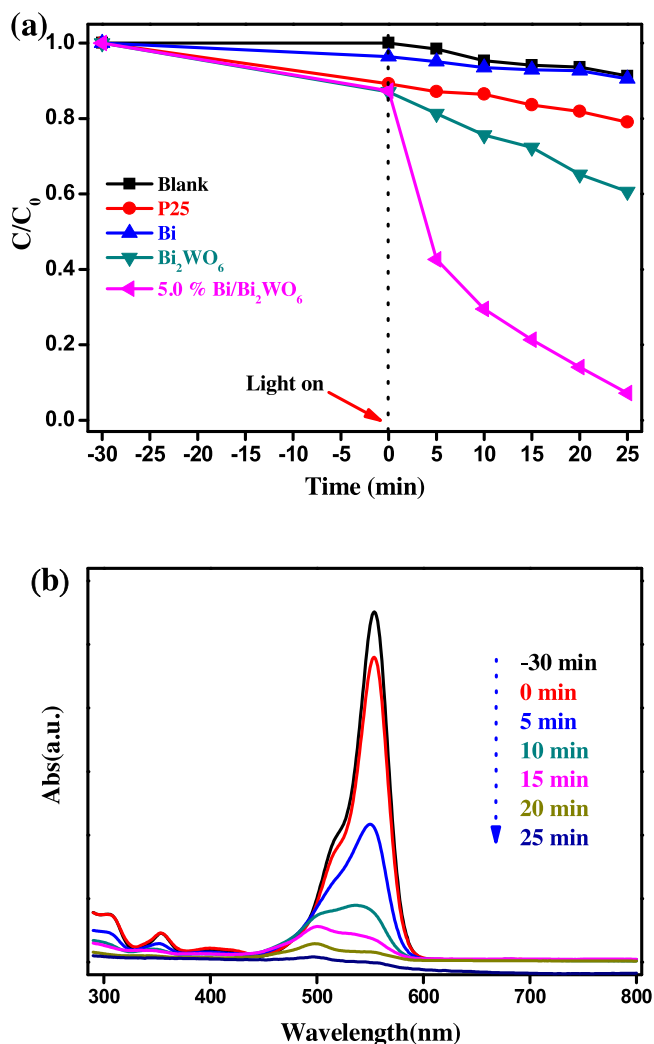


Fig. 7. Photocatalytic degradation of RhB by different photocatalysts under visible light irradiation (a), and changes in UV-vis absorption spectra of RhB by 5.0%  $\text{Bi/Bi}_2\text{WO}_6$  sample under visible light irradiation (b).

there is no obvious photodegradation by P25 under the same conditions. Obviously, metallic Bi has a negligible visible light activity on degradation of RhB. This result is supported by the fact that the photogenerated charge carriers in metallic Bi are insufficient to produce the active species under the same conditions [47]. When pure  $\text{Bi}_2\text{WO}_6$  is used as the photocatalyst, the photodegradation efficiency of RhB can just approach 39.0% after 25 min, indicating its low photocatalytic activity. However, when 5.0%  $\text{Bi/Bi}_2\text{WO}_6$  composites are used as the photocatalyst, the photodegradation rate is significantly improved compared with pure  $\text{Bi}_2\text{WO}_6$ . The remarkable visible photocatalytic activity of  $\text{Bi/Bi}_2\text{WO}_6$  is ascribed to the synergetic effect of Bi nanoparticles and  $\text{Bi}_2\text{WO}_6$ .

To further study the photocatalytic degradation process of RhB, the variation of the UV-vis spectrum of RhB degraded in the presence of 5.0%  $\text{Bi/Bi}_2\text{WO}_6$  is illustrated in Fig. 7b. The maximum absorbance shifted from 554 to 498 nm along with the rapid decrease of RhB absorption during the photodegradation process. These blue shifts can be ascribed to the de-ethylation process, suggesting a chemical change of RhB, other than adsorption during the degradation process [22,55]. The rapid decrease of RhB absorption is caused by the cleavage of the whole conjugated chromophore structure of RhB, which indicates that RhB can be efficiently degraded to small molecules or  $\text{CO}_2$ . These results demonstrate that both the N-deethylation process and the cleavage

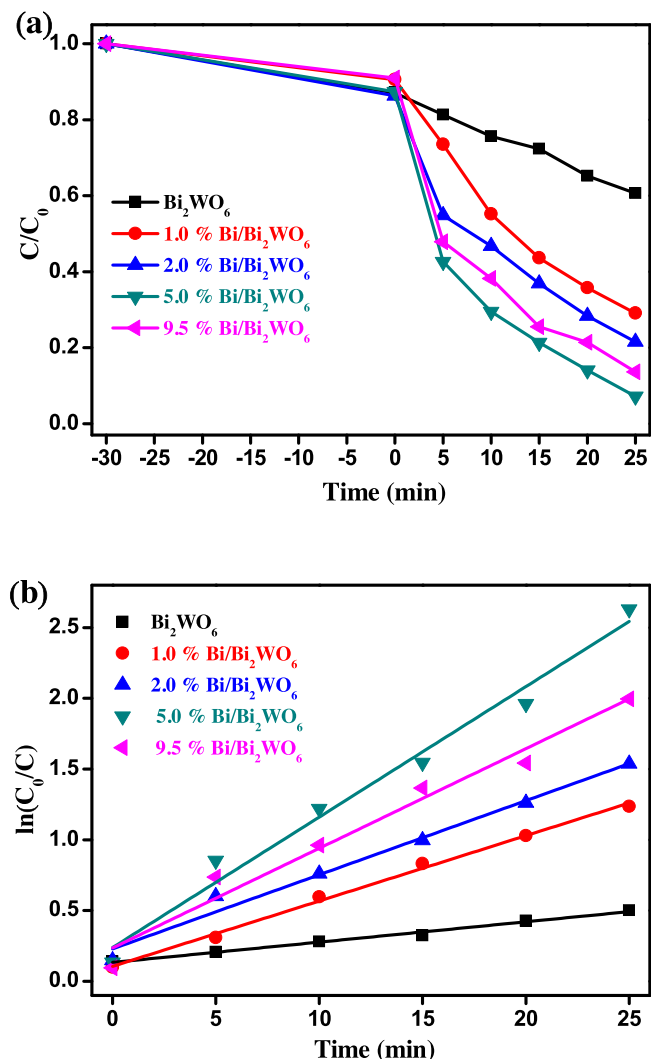


Fig. 8. Photocatalytic degradation of RhB by  $\text{Bi/Bi}_2\text{WO}_6$  composites with different percents of Bi under visible light irradiation, and (b) kinetic fit for the degradation of RhB with  $\text{Bi/Bi}_2\text{WO}_6$  composites with different percents of Bi.

of the conjugated chromophore structure occurred simultaneously during the photocatalytic reaction.

Furthermore, the effect of Bi content in the composite was also examined, as shown in Fig. 8a. As observed from Fig. 8a, the Bi content has a significant influence on the photocatalytic activity of the composites. The photocatalytic activity of  $\text{Bi/Bi}_2\text{WO}_6$  composite increased speedily with the increase in the amount of the metallic Bi from 1.0 to 5.0%, and thereafter it had a downtrend with further increase in the amount of metallic Bi. This may be because an insufficient Bi amount in  $\text{Bi/Bi}_2\text{WO}_6$  composite could not effectively separate photogenerated electrons and holes from heterojunction structures, giving rise to a low photocatalytic activity. On the other side, excess Bi on the surface of the  $\text{Bi}_2\text{WO}_6$  might offer as the recombination centers of electron-hole pairs, leading to a lower photocatalytic activity [31,48,50]. Notably, the 5.0%  $\text{Bi/Bi}_2\text{WO}_6$  composite exhibited the highest photocatalytic performance, and approximately 93.0% of the RhB was eliminated from the solution in 25 min. Owing to the low concentration of the RhB solution ( $10 \text{ mg L}^{-1}$ ), the photodegradation of RhB follows pseudo-first-order kinetics [12,34]. The first-order rate constant ( $k$ ) was calculated by the equation:  $\ln(C_0/C) = kt$ , where  $C_0$  and  $C$  are the concentration of RhB in aqueous solution at times 0 and  $t$ , and the slope  $k$  is the apparent reaction rate constant [26]. The kinetic



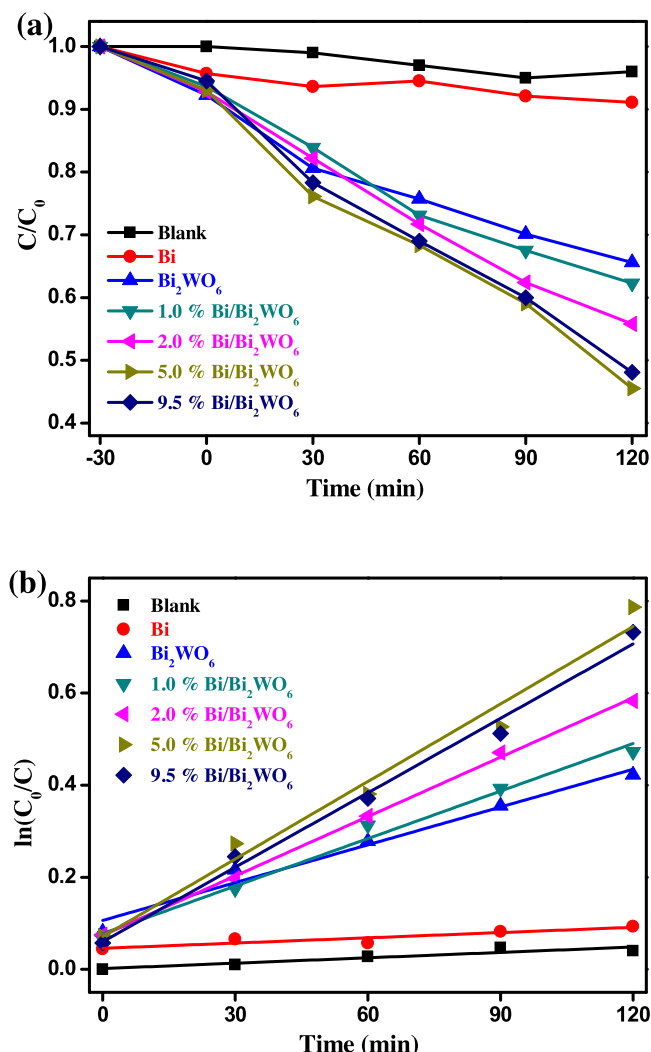


Fig. 9. Photocatalytic degradation of 4-CP by the  $\text{Bi/Bi}_2\text{WO}_6$  composites under visible light irradiation, and (b) kinetic fit for the degradation of 4-CP with the  $\text{Bi/Bi}_2\text{WO}_6$  composites.

curves were plotted and presented in Fig. 8b. The corresponding pseudo-first-order rate constants of the photodegradation of RhB over  $\text{Bi}_2\text{WO}_6$ , 1.0%  $\text{Bi/Bi}_2\text{WO}_6$ , 2.0%  $\text{Bi/Bi}_2\text{WO}_6$ , 5.0%  $\text{Bi/Bi}_2\text{WO}_6$ , and 9.5%  $\text{Bi/Bi}_2\text{WO}_6$ , are calculated to be 0.014, 0.046, 0.052, 0.092, and  $0.071 \text{ min}^{-1}$ , respectively. The 5.0%  $\text{Bi/Bi}_2\text{WO}_6$  composite exhibits a highest apparent reaction rate constant, which is in accordance with the curves of their photodegradation.

The photocatalytic performance of the  $\text{Bi/Bi}_2\text{WO}_6$  composites was also evaluated by the photodegradation of 4-CP (concentration of 20 mg/L) under visible light irradiation, as shown in Fig. 9a. It can be seen that for the blank sample, the photodegradation of 4-CP can be neglected during the whole visible-light irradiation, indicating that 4-CP is also a stable pollutant. The photodegradation of 4-CP are about 8.9% and 34.4% after 120 min of visible-light irradiation in the presence of the metallic Bi and  $\text{Bi}_2\text{WO}_6$ , respectively. Obviously, the  $\text{Bi/Bi}_2\text{WO}_6$  composites exhibit higher photocatalytic activity than the metallic Bi and  $\text{Bi}_2\text{WO}_6$ . Furthermore, the photocatalytic activity of  $\text{Bi/Bi}_2\text{WO}_6$  composite is strongly affected by the Bi content. Therefore, control over the content of metallic Bi is very crucial to photocatalytic activity of  $\text{Bi/Bi}_2\text{WO}_6$  composite. Similar to the photocatalytic degradation of RhB, the 5.0%  $\text{Bi/Bi}_2\text{WO}_6$  composite exhibits the highest photocatalytic activity, which presents 54.4% degradation efficiency after 120 min. The kinetics of 4-CP degrada-

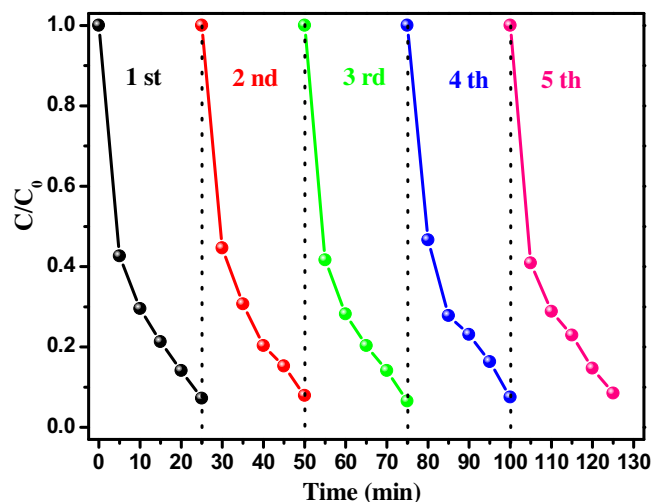


Fig. 10. Repeated experiments of photocatalytic degradation of RhB over the 5.0%  $\text{Bi/Bi}_2\text{WO}_6$  sample under visible light irradiation.

tion under visible light irradiation was also investigated (Fig. 9b). The apparent rate constants for  $\text{Bi}_2\text{WO}_6$ , 1.0%  $\text{Bi/Bi}_2\text{WO}_6$ , 2.0%  $\text{Bi/Bi}_2\text{WO}_6$ , 5.0%  $\text{Bi/Bi}_2\text{WO}_6$ , and 9.5%  $\text{Bi/Bi}_2\text{WO}_6$  are 0.0027, 0.0034, 0.0043, 0.0056, and  $0.0054 \text{ min}^{-1}$ , respectively. The photocatalytic activity of the 5.0%  $\text{Bi/Bi}_2\text{WO}_6$  composite was thus approximately two times higher than that of pure  $\text{Bi}_2\text{WO}_6$ . These results clearly reveal that the photocatalytic performance of 5.0%  $\text{Bi/Bi}_2\text{WO}_6$  heterojunction results from the excitation of the photocatalyst rather than the sensitization mechanism.

As the stability of photocatalysts is a general requirement for the practical application, the reusability of the 5.0%  $\text{Bi/Bi}_2\text{WO}_6$  composite was investigated. As shown in Fig. 10, after five recycles, no obvious loss of photocatalytic activity of the catalyst is observed. On the basis of XRD analysis of used sample and fresh sample (Fig. S3), it can be found that there is no obvious change in the crystalline phase of 5.0%  $\text{Bi/Bi}_2\text{WO}_6$  composite after the photocatalytic process, which is in line with its remarkable repeated photoactivity. These results demonstrate that the photocatalyst remained stable and active for repeated usage.

### 3.3. Photocatalytic mechanism

In order to further investigate the photocatalytic mechanism, the main active species generated during the decomposition process of RhB were inspected by the trapping experiments. Trapping of radicals and holes in experiments were performed using IPA, BQ, and EDTA as  $\cdot\text{OH}$  scavenger,  $\cdot\text{O}_2^-$  scavenger, and  $h^+$  scavenger, respectively [21,22]. Fig. 11 shows the effect of those scavengers on degradation of RhB using 5.0%  $\text{Bi/Bi}_2\text{WO}_6$  as the photocatalyst. It was found that in the presence of EDTA and BQ, the degradation rate was reduced to 25% and 43%, respectively. However, only a weak inhibition was observed on degradation of RhB with addition of IPA. Thus, it could be inferred that  $h^+$  and  $\cdot\text{O}_2^-$  should be the dominant active species in this photocatalytic system, while  $\cdot\text{OH}$  plays a minor role to photocatalytic reaction. Since the reduction potential of photogenerated electrons in  $\text{Bi}_2\text{WO}_6$  is higher than that of  $\cdot\text{O}_2^-/\text{O}_2$  (0.28 eV), the released electrons can easily transfer to the oxygen molecules ( $\text{O}_2$ ) adsorbed on the surface of the  $\text{Bi}_2\text{WO}_6$ , producing  $\cdot\text{O}_2^-$ , which is a strong oxidative species to degrade RhB molecules [12,21]. Additionally,  $\cdot\text{OH}$  cannot be directly produced by the photogenerated holes on the  $\text{Bi}_2\text{WO}_6$ . This is because the valence band position (+1.63 eV) of  $\text{Bi}_2\text{WO}_6$  is higher than that of  $\text{OH}/\text{OH}^+$  (1.99 eV), suggesting that holes on the surface of  $\text{Bi}_2\text{WO}_6$  could not react with  $\text{OH}^-/\text{H}_2\text{O}$  to form  $\cdot\text{OH}$  in photocatalytic reac-



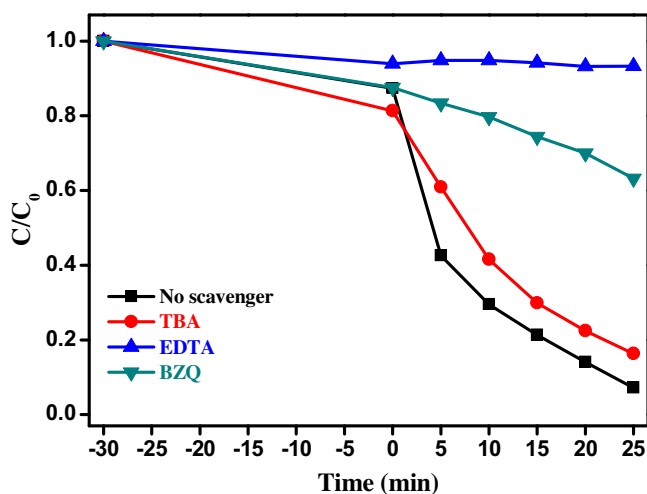


Fig. 11. Trapping experiment of active species during the photocatalytic degradation of RhB over 5.0% Bi/Bi<sub>2</sub>WO<sub>6</sub> under visible light irradiation.

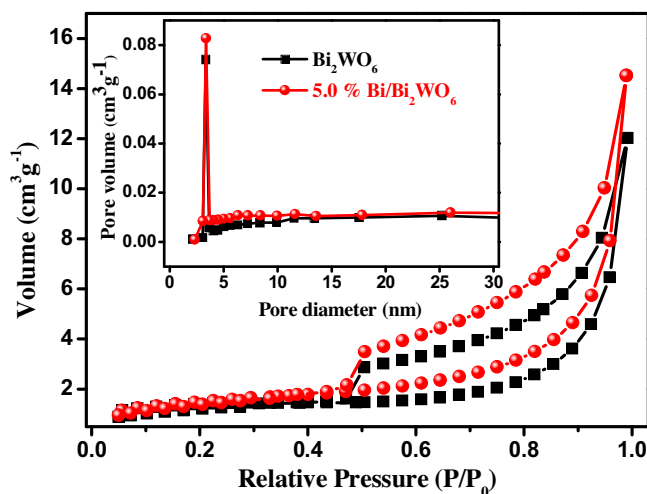


Fig. 12. Nitrogen adsorption-desorption isotherms and the corresponding pore size distribution plot (inset) of pure Bi<sub>2</sub>WO<sub>6</sub> and 5% Bi/Bi<sub>2</sub>WO<sub>6</sub>.

tion [12,29]. However, the  $\cdot\text{O}_2^-$ , with stronger reduction ability, can react with  $\text{H}_2\text{O}$  or  $\text{OH}^-$  to form  $\cdot\text{OH}$ . It is worth noting that the generation of  $\cdot\text{OH}$  is based on the amount of  $\cdot\text{O}_2^-$ , suggesting that  $\cdot\text{OH}$  plays a minor role for the degradation of RhB [23,29]. Therefore, the photogenerated holes and  $\cdot\text{O}_2^-$  radical are the predominant active species in this photocatalytic system, which coincides with the previous reports [56].

Generally, the large surface area for photocatalyst materials can provide more surface active sites for the adsorption of active species and reactant molecules, which makes the photocatalytic process more efficient [7]. The surface area and the porous structure of the samples were investigated by nitrogen adsorption-desorption isotherms. Fig. 12 shows nitrogen adsorption-desorption isotherms and the corresponding pore size distribution plot (inset) of the pure Bi<sub>2</sub>WO<sub>6</sub> and 5% Bi/Bi<sub>2</sub>WO<sub>6</sub> sample. The pure Bi<sub>2</sub>WO<sub>6</sub> has an adsorption-desorption isotherm of type IV with H3 hysteresis loops, implying the presence of mesopores in the size of 2–50 nm. This result can be further proved by the inset figure in Fig. 12, which indicates that the pore size mainly lies in the range of 2–4 nm. As can be seen, the adsorption-desorption isotherm and pore diameter distribution of the 5% Bi/Bi<sub>2</sub>WO<sub>6</sub> sample are similar to that of pure Bi<sub>2</sub>WO<sub>6</sub>. In addition, the specific surface area of the pure Bi<sub>2</sub>WO<sub>6</sub> and 5% Bi/Bi<sub>2</sub>WO<sub>6</sub> are calculated to be 4.92 m<sup>2</sup> g<sup>-1</sup> and 5.34 m<sup>2</sup> g<sup>-1</sup>,

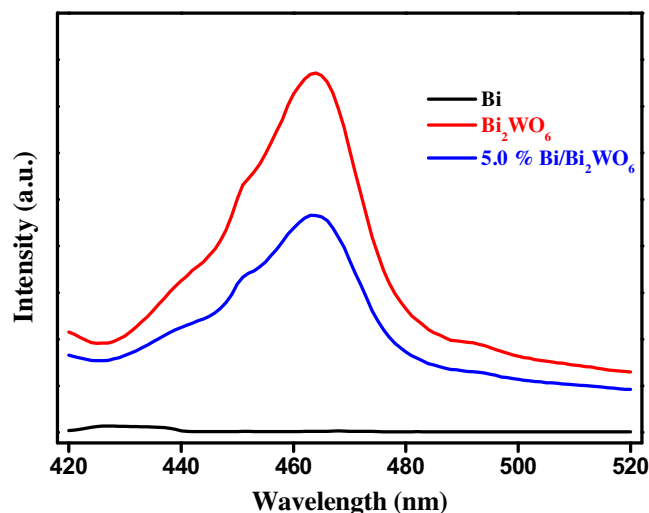
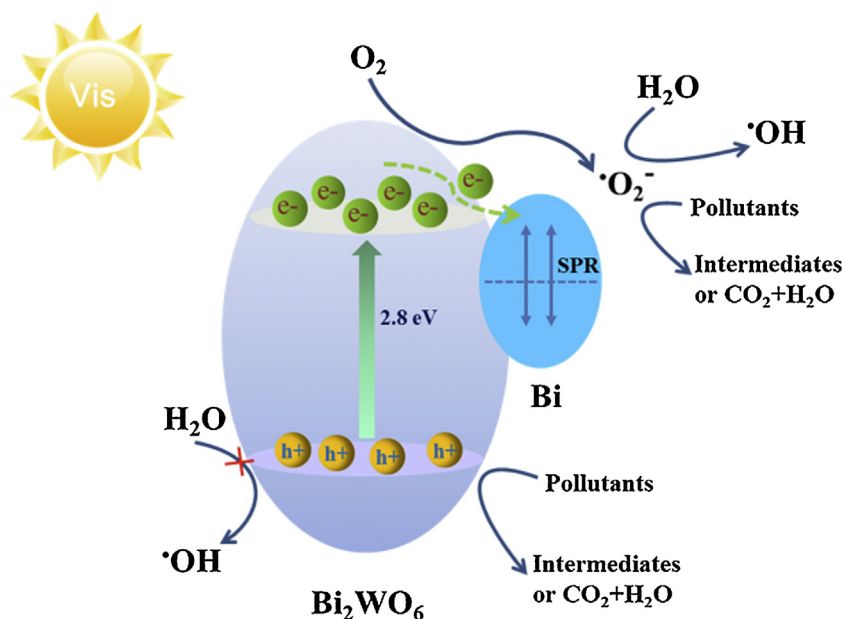


Fig. 13. Photoluminescence spectra of the metallic Bi, Bi<sub>2</sub>WO<sub>6</sub> and 5.0% Bi/Bi<sub>2</sub>WO<sub>6</sub> sample ( $\lambda_{\text{excitation}} = 300 \text{ nm}$ ).

respectively. It can be deduced that the specific surface areas and porosity play a minor role in the enhanced photocatalytic activity of the Bi/Bi<sub>2</sub>WO<sub>6</sub> composite.

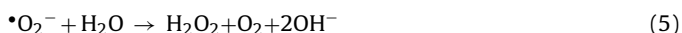
It has been widely accepted that the separation and transfer efficiency of photogenerated charge carrier of a photocatalyst play a crucial role in the photocatalytic reaction. Photoluminescence (PL) spectrum was applied to study the recombination of photogenerated electrons and holes in semiconductors [12,32]. Fig. 13 shows the PL spectrum of the metallic Bi, Bi<sub>2</sub>WO<sub>6</sub> and 5.0% Bi/Bi<sub>2</sub>WO<sub>6</sub> in the range of 400–520 nm excited with a wavelength of 300 nm. The PL spectra of the pure Bi<sub>2</sub>WO<sub>6</sub> reveal that strong emission peak appeared at around 465 nm owing to the intrinsic luminescence of Bi<sub>2</sub>WO<sub>6</sub> [12,57]. In contrast, it can be noted that the metallic Bi displays the lowest intensity. This phenomenon can be interpreted as that the relatively low amount of photogenerated electrons and holes are formed under the same conditions. A similar phenomenon has been reported in the red phosphor and BiOBr materials [58,59]. The PL spectra of the pure Bi<sub>2</sub>WO<sub>6</sub> and 5.0% Bi/Bi<sub>2</sub>WO<sub>6</sub> sample show the main peaks at similar positions but with different intensities. Moreover, the emission intensity of the 5.0% Bi/Bi<sub>2</sub>WO<sub>6</sub> sample is obviously lower than that of the pure Bi<sub>2</sub>WO<sub>6</sub>, indicating that the recombination of electrons and holes is inhibited in the 5.0% Bi/Bi<sub>2</sub>WO<sub>6</sub> sample. The results are in consistent with the result from photodegradation experiment.

Based on the above experimental results and the theory analysis, the reaction mechanism of photocatalytic degradation of RhB upon Bi/Bi<sub>2</sub>WO<sub>6</sub> was presented in Scheme 1. When Bi nanoparticles with diameters in the range of 5–15 nm are deposited on the surface of Bi<sub>2</sub>WO<sub>6</sub> nanosheet, a Schottky barrier would be established at their interface due to the difference in work functions [35,60,61]. Generally, the direct electron transfer depends on the alignment of the band levels of the semiconductor and Fermi level of the plasmonic metal [7,61]. According to literature [29,62], the conduction band of Bi<sub>2</sub>WO<sub>6</sub> is about  $-1.04 \text{ eV}$  (vs. NHE), which is much more negative than the Fermi level of metal Bi ( $-0.17 \text{ eV}$ ). This suggests that the photoexcited electrons could transfer from Bi<sub>2</sub>WO<sub>6</sub> to metal Bi, which is consistent with the previous study on electron transfer from the semiconductor to the plasmonic metal [21,44,47,60]. Due to excellent intrinsic physical and chemical properties, Bi<sub>2</sub>WO<sub>6</sub> can be easily excited under visible light irradiation to generate the photogenerated electrons in the conduction band and holes in the valence band, respectively [11,52]. Owing to their Schottky barriers at the metal-semiconductor interface, parts of the photogenerated



**Scheme 1.** The proposed photocatalytic mechanism for photodegradation of organic pollutants over the Bi/Bi<sub>2</sub>WO<sub>6</sub> composite.

electrons formed on the conduction band of Bi<sub>2</sub>WO<sub>6</sub> can transfer to Bi nanoparticles, thus reducing the recombination possibility with photogenerated holes [31,38,39]. Furthermore, the electron-hole generation rate in the Bi<sub>2</sub>WO<sub>6</sub> greatly increases because of the SPR-induced local electromagnetic field in the metallic Bi nanoparticles [38,49]. Finally, these separated electrons and holes will result in the degradation of organic contaminant. The photocatalytic reaction possibly includes the following:



## 5. Conclusions

Bi nanoparticles with a size of 5–15 nm are uniformly deposited on the surface of Bi<sub>2</sub>WO<sub>6</sub> microspheres by a simple solvothermal method to form the Bi/Bi<sub>2</sub>WO<sub>6</sub> composite. The photocatalytic activity of Bi/Bi<sub>2</sub>WO<sub>6</sub> was greatly enhanced compared with Bi nanoparticles and pure Bi<sub>2</sub>WO<sub>6</sub>. The content of metallic Bi has an impact on the catalytic activity of Bi/Bi<sub>2</sub>WO<sub>6</sub> composite. The 5.0% Bi/Bi<sub>2</sub>WO<sub>6</sub> exhibited the best photocatalytic activity. Radical species experiments confirmed the holes and •O<sub>2</sub><sup>−</sup> were the main reactive species for the photocatalytic degradation of RhB. Moreover, the Bi/Bi<sub>2</sub>WO<sub>6</sub> composite exhibited excellent reusability under visible-light irradiation. The PL results confirmed that Bi loading greatly improved the effective separation and migration of photogenerated carriers, thereby increasing the lifetime of the electron-hole separation. The enhanced photocatalytic activity should be attributed to synergetic effect of Bi nanoparticles and Bi<sub>2</sub>WO<sub>6</sub>, which resulted in enhanced adsorption of visible light, effective separation and migration of photogenerated carriers, and reduced recombination of photogenerated electron-hole

pairs. The study is helpful for the design of novel and highly efficient visible-light-driven metal-semiconductor photocatalysts for environmental remediation.

## Acknowledgements

This work was carried out with financial supports from National Natural Science Foundation of China (61171008 and 21103024). This research was also supported by Yancheng Huanbo Energy Technology Co., Ltd and Shanghai Jubo Energy Technology Co., Ltd on field and fund.

## Appendix A. Supplementary data

Supplementary data associated with this article can be found, in the online version, at <http://dx.doi.org/10.1016/j.apcatb.2016.05.022>.

## References

- [1] M.Y. Guo, A.M.C. Ng, F. Liu, A.B. Djurišić, W.K. Chan, *Appl. Catal. B: Environ.* 107 (2011) 150–157.
- [2] C. Chen, W. Ma, J. Zhao, *Chem. Soc. Rev.* 39 (2010) 4206–4219.
- [3] X. Lang, X. Chen, J. Zhao, *Chem. Soc. Rev.* 43 (2014) 473–486.
- [4] S. Banerjee, S.C. Pillai, P. Falaras, K.E. O'Shea, J.A. Byrne, D.D. Dionysiou, *J. Phys. Chem. Lett.* 5 (2014) 2543–2554.
- [5] H. Tong, S. Ouyang, Y. Bi, N. Umezawa, M. Oshikiri, J. Ye, *Adv. Mater.* 24 (2012) 229–251.
- [6] G. Liu, L. Wang, H.G. Yang, H.-M. Cheng, G.Q. Lu, *J. Mater. Chem.* 20 (2010) 831–843.
- [7] J. Tian, Z. Zhao, A. Kumar, R.I. Boughton, H. Liu, *Chem. Soc. Rev.* 43 (2014) 6920–6937.
- [8] Q. Zhang, D.Q. Lima, I. Lee, F. Zaera, M. Chi, Y. Yin, *Angew. Chem. Int. Ed. Engl.* 50 (2011) 7088–7092.
- [9] D. Zhang, G. Li, H. Li, Y. Lu, *Chem. Asian. J.* 8 (2013) 26–40.
- [10] J. Li, Y. Yu, L. Zhang, *Nanoscale* 6 (2014) 8473–8488.
- [11] L.S. Zhang, H.L. Wang, Z.G. Chen, P.K. Wong, J.S. Liu, *Appl. Catal. B: Environ.* 106 (2011) 1–13.
- [12] D. Wang, L. Guo, Y. Zhen, L. Yue, G. Xue, F. Fu, *J. Mater. Chem. A* 2 (2014) 11716–11727.
- [13] L. Zhang, Y. Zhu, *Catal. Sci. Technol.* 2 (2012) 694–706.
- [14] H. Xie, D. Shen, X. Wang, G. Shen, *Mater. Chem. Phys.* 103 (2007) 334–339.
- [15] Q. Sun, X. Jia, X. Wang, H. Yu, J. Yu, *Dalton. Trans.* 44 (2015) 14532–14539.
- [16] J. He, W. Wang, F. Long, Z. Zou, Z. Fu, Z. Xu, *Mater. Sci. Eng. B* 177 (2012) 967–974.
- [17] Y. Li, J. Liu, X. Huang, G. Li, *Cryst. Growth Des.* 7 (2007) 1350–1355.
- [18] Z. Cui, D. Zeng, T. Tang, J. Liu, C. Xie, *J. Hazard. Mater.* 183 (2010) 211–217.

- [19] X. Wang, L. Chang, J. Wang, N. Song, H. Liu, X. Wan, *Appl. Surf. Sci.* 270 (2013) 685–689.
- [20] G. Zhang, Z. Hu, M. Sun, Y. Liu, L. Liu, H. Liu, C.-P. Huang, J. Qu, J. Li, *Adv. Funct. Mater.* 25 (2015) 3726–3734.
- [21] J. Ren, W.Z. Wang, S.M. Sun, L. Zhang, J. Chang, *Appl. Catal. B: Environ.* 92 (2009) 50–55.
- [22] J. Xia, J. Di, S. Yin, H. Xu, J. Zhang, Y. Xu, L. Xu, H. Li, M. Ji, *RSC Adv.* 4 (2014) 82–90.
- [23] N. Tian, Y. Zhang, H. Huang, Y. He, Y. Guo, *J. Phys. Chem. C* 118 (2014) 15640–15648.
- [24] X.C. Song, Y.F. Zheng, R. Ma, Y.Y. Zhang, H.Y. Yin, *J. Hazard. Mater.* 192 (2011) 186–191.
- [25] J. Huang, G. Tan, H. Ren, W. Yang, C. Xu, C. Zhao, A. Xia, *ACS Appl. Mater. Interfaces* 6 (2014) 21041–21050.
- [26] H. Huang, K. Liu, K. Chen, Y. Zhang, Y. Zhang, S. Wang, *J. Phys. Chem. C* 118 (2014) 14379–14387.
- [27] M. Shang, W.Z. Wang, L. Zhang, H.L. Xu, *Mater. Chem. Phys.* 120 (2010) 155–159.
- [28] J. Tian, Y. Sang, G. Yu, H. Jiang, X. Mu, H. Liu, *Adv. Mater.* 25 (2013) 5075–5080.
- [29] Y. Liu, B. Wei, L. Xu, H. Gao, M. Zhang, *ChemCatChem* 7 (2015) 4076–4084.
- [30] L. Ge, J. Liu, *Appl. Catal. B: Environ.* 105 (2011) 289–297.
- [31] L. Sun, R. Zhang, Y. Wang, W. Chen, *ACS Appl. Mater. Interfaces* 6 (2014) 14819–14826.
- [32] Z. Lian, W. Wang, S. Xiao, X. Li, Y. Cui, D. Zhang, G. Li, H. Li, *Sci. Rep.* 5 (2015) 10461.
- [33] K. Mori, P. Verma, R. Hayashi, K. Fuku, H. Yamashita, *Chem. Eur. J.* 21 (2015) 11885–11893.
- [34] L. Wu, F. Li, Y. Xu, J.W. Zhang, D. Zhang, G. Li, H. Li, *Appl. Catal. B: Environ.* 164 (2015) 217–224.
- [35] H. Cheng, K. Fuku, Y. Kuwahara, K. Mori, H. Yamashita, *J. Mater. Chem. A* 3 (2015) 5244–5258.
- [36] J. Yang, X. Wang, Y. Chen, J. Dai, S. Sun, *RSC Adv.* 5 (2015) 9771–9782.
- [37] Q.-S. Wu, Y. Cui, L.-M. Yang, G.-Y. Zhang, D.-Z. Gao, *Sep. Purif. Technol.* 142 (2015) 168–175.
- [38] J. Low, J. Yu, Q. Li, B. Cheng, *Phys. Chem. Chem. Phys.* 16 (2014) 1111–1120.
- [39] C. Yu, Y. Bai, J. Chen, W. Zhou, H. He, J.C. Yu, L. Zhu, S. Xue, *Sep. Purif. Technol.* 154 (2015) 115–122.
- [40] S. Sun, W. Wang, L. Zhang, *J. Phys. Chem. C* 117 (2013) 9113–9120.
- [41] F. Dong, T. Xiong, Y. Sun, Z. Zhao, Y. Zhou, X. Feng, Z. Wu, *Chem. Commun.* 50 (2014) 10386–10389.
- [42] Y. Wang, J. Chen, L. Chen, Y.-B. Chen, L.-M. Wu, *Cryst. Growth Des.* 10 (2010) 1578–1584.
- [43] Z. Wang, C. Jiang, R. Huang, H. Peng, X. Tang, *J. Phys. Chem. C* 118 (2014) 1155–1160.
- [44] Y. Chen, D. Chen, J. Chen, Q. Lu, M. Zhang, B. Liu, Q. Wang, Z. Wang, *J. Alloy. Compd.* 651 (2015) 114–120.
- [45] Y.W. Wang, J.S. Kim, G.H. Kim, K.S. Kim, *Appl. Phys. Lett.* 88 (2006) 143106.
- [46] X. Liu, H. Cao, J. Yin, *Nano Res.* 4 (2011) 470–482.
- [47] F. Dong, Q. Li, Y. Sun, W.-K. Ho, *ACS Catal.* 4 (2014) 4341–4350.
- [48] S. Weng, B. Chen, L. Xie, Z. Zheng, P. Liu, *J. Mater. Chem. A* 1 (2013) 3068–3075.
- [49] Y. Yu, C. Cao, H. Liu, P. Li, F. Wei, Y. Jiang, W. Song, *J. Mater. Chem. A* 2 (2014) 1677–1681.
- [50] H. Gnyam, Y. Sasson, *J. Phys. Chem. C* 119 (2015) 19201–19209.
- [51] M. Crane, R.L. Frost, P.A. Williams, J. Theo Klopogge, *J. Raman, Spectrosc* 33 (2002) 62–66.
- [52] J. Yang, X. Wang, X. Zhao, J. Dai, S. Mo, *J. Phys. Chem. C* 119 (2015) 3068–3078.
- [53] Y. Zhou, Y. Zhang, M. Lin, J. Long, Z. Zhang, H. Lin, J.C. Wu, X. Wang, *Nat. Commun.* 6 (2015) 8340.
- [54] C. Li, G. Chen, J. Sun, Y. Feng, J. Liu, H. Dong, *Appl. Catal. B: Environ.* 163 (2015) 415–423.
- [55] Y. Huo, X. Chen, J. Zhang, G. Pan, J. Jia, H. Li, *Appl. Catal. B: Environ.* 148–149 (2014) 550–556.
- [56] C. Li, G. Chen, J. Sun, H. Dong, Y. Wang, C. Lv, *Appl. Catal. B: Environ.* 160–161 (2014) 383–389.
- [57] D. Wang, G. Xue, Y. Zhen, F. Fu, D. Li, *J. Mater. Chem.* 22 (2012) 4751.
- [58] Y.-P. Yuan, S.-W. Cao, Y.-S. Liao, L.-S. Yin, C. Xue, *Appl. Catal. B: Environ.* 140–141 (2013) 164–168.
- [59] Y. Sun, W. Zhang, T. Xiong, Z. Zhao, F. Dong, R. Wang, W.K. Ho, *J. Colloid Interface Sci.* 418 (2014) 317–323.
- [60] A. Furube, L. Du, K. Hara, R. Katoh, M. Tachiya, *J. Am. Chem. Soc.* 129 (2007) 14852–14853.
- [61] Y. Zheng, L. Zheng, Y. Zhan, X. Lin, Q. Zheng, K. Wei, *Inorg. Chem.* 46 (2007) 6980–6986.
- [62] Y. Zhang, N. Zhang, Z.-R. Tang, Y.-J. Xu, *Chem. Sci.* 4 (2013) 1820–1824.